Research Article | Vol. 26, No. 4 | 19 Feb 2018 | OPTICS EXPRESS 4194
Optics EXPRESS

# Quasi-phase-matched second harmonic generation of long-range surface plasmon polaritons

GUO-XIN CUI,[1] ZI-JIAN WU,[1] MENG-YING WANG,[1] YANG MING,[1] ZHENG XING,[2] KAI QIU,[3] LIE-RONG YUAN,[3] JUN TAN,[3] XUE-JIN ZHANG,[1] AND YAN-QING LU[1,*]

[1]*National Laboratory of Solid State Microstructures, College of Engineering and Applied Sciences, Nanjing University, Nanjing 210093, China*
[2]*Key Laboratory of Nanodevices and Applications, Suzhou Institute of Nano-tech and Nano-Bionics, Chinese Academy of Sciences, Suzhou 215123, China*
[3]*National Laboratory of Solid State Microstructures, School of Physics, Nanjing University, Nanjing 210093, China*
**yqlu@nju.edu.cn*

**Abstract:** In this paper, we experimentally demonstrate the second harmonic generation of long-range surface plasmon polaritons via quasi-phase matching in lithium niobate. After depositing a 9/13 nm thick Au film on periodically poled lithium niobate, $TiO_2$ of about 2.3 μm in thickness is evaporated on the sample as a refractive-index-matching material. This dielectric (periodically poled lithium niobate)–metal(Au)–dielectric($TiO_2$) sandwich structure can support the transmission of long-range surface plasmon polaritons through it. By designing a moderate ferroelectric domain period of periodically poled lithium niobate, the phase mismatch between the fundamental wave and second harmonic wave of the long-range surface plasmon polaritons can be compensated and a second harmonic wave can be generated effectively. This can be used to provide integrated plasmonic devices with attractive applications in quantum and classic information processing.



**OCIS codes:** (130.3730) Lithium niobate; (190.2620) Harmonic generation and mixing; (240.6680) Surface plasmons.

## References and links

1. A. Drezet, D. Koller, A. Hohenau, A. Leitner, F. R. Aussenegg, and J. R. Krenn, "Plasmonic crystal demultiplexer and multiports," Nano Lett. **7**(6), 1697–1700 (2007).
2. L. Li, T. Li, S. M. Wang, C. Zhang, and S. N. Zhu, "Plasmonic Airy beam generated by in-plane diffraction," Phys. Rev. Lett. **107**(12), 126804 (2011).
3. S. M. Wang, Q. Q. Cheng, Y. X. Gong, P. Xu, C. Sun, L. Li, T. Li, and S. N. Zhu, "A 14 × 14 μm$^2$ footprint polarization-encoded quantum controlled-NOT gate based on hybrid waveguide," Nat. Commun. **7**, 11490 (2016).
4. I. Epstein, Y. Tsur, and A. Arie, "Surface plasmons wavefront and spectral shaping by near-field holography," Laser Photonics Rev. **10**(3), 360–381 (2016).
5. A. V. Zayats, I. I. Smolyaninov, and A. A. Maradudin, "Nano-optics of surface plasmon polaritons," Phys. Rep. **408**(3–4), 131–314 (2005).
6. L. Novotny and N. van Hulst, "Antennas for light," Nat. Photonics **5**(2), 83–90 (2011).
7. C. M. Soukoulis and M. Wegener, "Past achievements and future challenges in the development of three-dimensional photonic metamaterials," Nat. Photonics **5**(9), 523–530 (2011).
8. M. S. Tame, K. R. McEnery, Ş. K. Özdemir, J. Lee, S. A. Maier, and M. S. Kim, "Quantum plasmonics," Nat. Phys. **9**(6), 329–340 (2013).
9. Y. Ming, W. Zhang, Z. Chen, Z. Wu, J. Tang, F. Xu, L. Zhang, and Y. Lu, "Squeezing a surface plasmon through quadratic nonlinear interactions," ACS Photonics **3**(11), 2074–2082 (2016).
10. A. Ji, T. V. Raziman, J. Butet, R. P. Sharma, and O. J. Martin, "Optical forces and torques on realistic plasmonic nanostructures: a surface integral approach," Opt. Lett. **39**(16), 4699–4702 (2014).
11. T. V. Raziman and O. J. F. Martin, "Internal optical forces in plasmonic nanostructures," Opt. Express **23**(15), 20143–20157 (2015).
12. F. Yang and Z. Lei Mei, "Guiding SPPs with PT-symmetry," Sci. Rep. **5**(1), 14981 (2015).

#312930 https://doi.org/10.1364/OE.26.004194
Journal © 2018 Received 8 Nov 2017; revised 2 Feb 2018; accepted 4 Feb 2018; published 8 Feb 2018

Optics EXPRESS

13. M. Kauranen and A. V. Zayats, "Nonlinear plasmonics," Nat. Photonics **6**(11), 737–748 (2012).
14. J. Yao and Y. Wang, "Quasi-phase matching technology," in *Nonlinear Optics and Solid-State Lasers*, pp. 319–382 (2011).
15. B. Yang, Y. Y. Yue, R. E. Lu, X. H. Hong, C. Zhang, Y. Q. Qin, and Y. Y. Zhu, "Rigorous intensity and phase-shift manipulation in optical frequency conversion," Sci. Rep. **6**(1), 27457 (2016).
16. Z. Qi, T. Li, and S. N. Zhu, "highly-confined second harmonic generation in nano-scale slot waveguides," J. Phys. D Appl. Phys. **41**(2), 025109 (2008).
17. A. Rose and D. R. Smith, "Broadly tunable quasi-phase-matching in nonlinear metamaterials," Phys. Rev. A **84**(1), 013823 (2011).
18. A. Rose, D. Huang, and D. R. Smith, "Controlling the second harmonic in a phase-matched negative-index metamaterial," Phys. Rev. Lett. **107**(6), 063902 (2011).
19. N. Mattiucci, M. J. Bloemer, and G. D'Aguanno, "Phase-matched second harmonic generation at the Dirac point of a 2-D photonic crystal," Opt. Express **22**(6), 6381–6390 (2014).
20. P. Berini, "Long-range surface plasmon polaritons," Adv. Opt. Photonics **1**(1), 484–588 (2009).
21. S. A. Maier, *Plasmonics: Fundamentals and Applications* (Springer, 2007).
22. Z. J. Wu, X. K. Hu, Z. Y. Yu, W. Hu, F. Xu, and Y. Q. Lu, "Nonlinear plasmonic frequency conversion through quasi-phase matching," Phys. Rev. B **82**(15), 155107 (2010).
23. D. H. Jundt, "Temperature-dependent Sellmeier equation for the index of refraction, $n_e$, in congruent lithium niobate," Opt. Lett. **22**(20), 1553–1555 (1997).
24. D. Wei, Y. Zhu, W. Zhong, G. Cui, H. Wang, Y. He, Y. Zhang, Y. Lu, and M. Xiao, "Directly generating orbital angular momentum in second-harmonic waves with a spirally poled nonlinear photonic crystal," Appl. Phys. Lett. **110**(26), 261104 (2017).
25. M. Levy, R. M. Osgood, Jr., R. Liu, L. E. Cross, G. S. Cargill III, A. Kumar, and H. Bakhru, "Fabrication of single-crystal lithium niobate films by crystal ion slicing," Appl. Phys. Lett. **73**(16), 2293–2295 (1998).
26. NANOLN, (http://www.nanoln.com/en/).
27. T. A. Rost, H. Lin, T. A. Rabson, R. C. Baumann, and D. L. Callahan, "Deposition and analysis of lithium niobate and other lithium niobium oxides by rf magnetron sputtering," J. Appl. Phys. **72**(9), 4336–4343 (1992).
28. R. J. Isaifan, A. Samara, W. Suwaileh, D. Johnson, W. Yiming, A. A. Abdallah, and B. Aïssa, "Improved self-cleaning properties of an efficient and easy to scale up $TiO_2$ thin films prepared by adsorptive self-assembly," Sci. Rep. **7**(1), 9466 (2017).
29. N. Mattiucci, G. D'Aguanno, and M. J. Bloemer, "Long range plasmon assisted all-optical switching at telecommunication wavelengths," Opt. Lett. **37**(2), 121–123 (2012).
30. Z. D. Gao, S. N. Zhu, S. Y. Tu, and A. H. Kung, "Monolithic red-green-blue laser light source based on cascaded wavelength conversion in periodically poled stoichiometric lithium tantalite," Appl. Phys. Lett. **89**(18), 181101 (2006).
31. W. Wan, J. Gao, and X. Yang, "Full-color plasmonic metasurface holograms," ACS Nano **10**(12), 10671–10680 (2016).
32. M. Lapine, I. V. Shadrivov, and Y. S. Kivshar, "Colloquium: Nonlinear metamaterials," Rev. Mod. Phys. **86**(3), 1093–1123 (2014).
33. H. Jin, P. Xu, X. W. Luo, H. Y. Leng, Y. X. Gong, W. J. Yu, M. L. Zhong, G. Zhao, and S. N. Zhu, "Compact engineering of path-entangled sources from a monolithic quadratic nonlinear photonic crystal," Phys. Rev. Lett. **111**(2), 023603 (2013).
34. H. Jin, F. M. Liu, P. Xu, J. L. Xia, M. L. Zhong, Y. Yuan, J. W. Zhou, Y. X. Gong, W. Wang, and S. N. Zhu, "On-chip generation and manipulation of entangled photons based on reconfigurable lithium-niobate waveguide circuits," Phys. Rev. Lett. **113**(10), 103601 (2014).

## 1. Introduction

With the rapid development of semiconductor manufacturing technology, plasmonics has attracted significant attention in the past few years. Surface plasmon polaritons (SPPs) can transmit or manipulate signals at the sub-micrometer or nanometer scale at optical frequencies because of their inherent properties, enabling SPPs to have many potential applications in integrated optics. Several SPP photonic devices have been reported, such as plasmonic demultiplexers [1], Airy beams [2], and polarization-encoded quantum-controlled NOT gates [3]. In addition, new theories, concepts, and applications of SPPs have emerged, including SPP holography [4], SPP crystals [5], nano-antennae [6], and plasmonic metamaterials [7]. Quantum plasmonics [8,9] has been studied extensively and some researchers have been focused on the optical force of plasmonic nanostructures [10,11]. F. Yang *et al.* proposed a method to guide SPPs with PT symmetry [12]. The nonlinear effect is an important phenomenon and is exhibited by plasmonics [13]. In addition, second harmonic generation (SHG) is a typical quadratic nonlinear effect. However, researchers have mainly focused on the SHG and enhancement of the localized surface plasmons (LSPs) of nanoparticles and

Optics EXPRESS

nanostructures. Because of the strong absorption of metals at optical frequencies, the SHG efficiency of LSPs is low and the typical transmission distance of the SHG of LSPs ranges from sub-micrometers to micrometers [13]. The size of integrated photonic devices/chips usually ranges from about tens of micrometers to millimeters [3]. Therefore, if we design nonlinear integrated photonic devices/chips based on the SHG of SPPs, the efficiency and transmission distance of SHGs should both improve greatly.

Quasi-phase matching (QPM) is a popular method to realize SHG effectively [14]. A widely used QPM crystal is periodically poled lithium niobate (PPLN), and in bulk crystals, QPM helps to realize very-high-efficiency SHG (~100%) [15]. Recently, a lot of new photonic phenomena and devices were brought up, and these greatly extended the application fields of QPM. High-confined QPM SHG in many micro/nano structures has been reported. For example, a nano-scale slot waveguide was proposed to enhance the SHG efficiency [16]. QPM was used to realize SHG at THz [17] and microwave [18] frequencies in nonlinear metamaterials. QPM SHG at the Dirac-point of 2-D photonic crystals was revealed with many promising applications [19].

To achieve a long transmission distance of SPP SHG, long-range surface plasmon polaritons (LRSPPs) are necessary [20]. A sandwich structure such as a dielectric–metal–dielectric (DMD) can support LRSPPs transmission [21]. When SPPs are transmitting along these sandwich structures, if the metal layer is sufficiently thin, the SPPs at the top and bottom interfaces of the metal will couple and form a stable mode. When SPPs at the two interfaces are symmetrical, most of the SPP energy will transmit in the dielectric layers, leaving only a little energy in the metal layer, which will suffer from strong absorption. Therefore, this SPP mode exhibits a much longer transmission distance of hundreds of micrometers or even millimeters. The thinner the metal layer, the lower the confinement of the coupled SPP and the larger the transmission distance. This is why LRSPPs exhibit much longer transmission distance than LSPs.

In this paper, we present our experiment on the QPM SHG of LRSPPs. To obtain SPP SHG with a high efficiency and large transmission distance, we consider a DMD structure with PPLN as the substrate, an Au film as the metal, and $TiO_2$ as the top dielectric layer, which is used to match the extraordinary refractive index (RI) ($n_e$) of lithium niobate ($LiNbO_3$) so LRSPPs can be generated. With this design, the efficiency and transmission distance of the SPP SHG can be improved effectively.

## 2. Theory

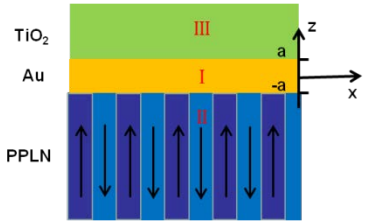


Fig. 1. Schematic of the sample.

Figure 1 shows a schematic of the sample. PPLN with a thickness of 50 μm is used as the substrate of the sample. Then, a thin Au film is deposited on the PPLN film. Finally, $TiO_2$ is evaporated as a RI-matching material. In the LRSPPs, the transmission constant is related to the thickness of the Au film, whereas the ferroelectric domain period of PPLN is determined by the phase of the fundamental wave (FW) and second harmonic (SH) wave in QPM. Thus, to realize QPM, the period of PPLN should be matched to the thickness of the Au film. In contrast, because the electric component $E_x$ is much smaller than $E_z$, the $E_z$ and $d_{33}$ component of the nonlinear coefficient of $LiNbO_3$ are used to calculate the electric field of the SH of LRSPPs in coupling wave theory. Therefore, we set the RI of $TiO_2$ equal to the $n_e$ of $LiNbO_3$

Optics EXPRESS

both at the FW and SH. We can calculate the period of the PPLN with the field continuum theory described in [21]. Only transverse magnetic (TM) waves can excite LRSPPs. Based on Maxwell's equations, the wave propagation equation, and the continuum of $E_x$ and $H_y$ at the interfaces of the metal, we can obtain

$$e^{4k_1 a} = \frac{k_1/\varepsilon_1 - k_2/\varepsilon_{2o}}{k_1/\varepsilon_1 + k_2/\varepsilon_{2o}} \cdot \frac{k_1/\varepsilon_1 - k_3/\varepsilon_3}{k_1/\varepsilon_1 + k_3/\varepsilon_3}. \tag{1}$$

In this equation, $k_i$ (i = I, II, III in Fig. 1) is the wave vector of different layers and $\varepsilon_i$ is the permittivity. $\varepsilon_{2o}$ and $\varepsilon_{2e}$ are the ordinary and extraordinary permittivities of $LiNbO_3$, respectively, while $2a = d$ is the thickness of the Au film.

Between the wave vector $k_i$ and transmission constant $\beta$ of the LRSPPs, we have

$$k_i^2 = \beta^2 - k_0^{\,2}\varepsilon_i, \quad \text{i = I, III when the layer is an isotropic material,} \tag{2}$$

$$k_i^2 = \frac{\varepsilon_{2o}}{\varepsilon_{2e}}\beta^2 - k_i^{\,2}\varepsilon_{2o}, \quad \text{i = II when } LiNbO_3 \text{ is an anisotropic material.} \tag{3}$$

Combining Eqs. (1)-(3), we can calculate the transmission constants $\beta$ of the FW and SH. It should be noted here that the $\beta$ of LRSPPs is complex; the imaginary part represents the absorption of the LRSPPs. Thus, the QPM condition in LRSPPs is different from traditional QPM. The simplified coupling equation of LRSPPs over PPLN can be written as (Eq. (4) in [22])

$$\begin{aligned} \frac{d}{dx}a^w(x) &= i\frac{w}{4}a^{2w}a^{w*}e^{i(\beta^{2w}-\beta^{w*}-\beta^w)x}\varepsilon_0\int E_z^{2w}(E_z^{w*})^2 d_{33}(x,z)dz, \\ \frac{d}{dx}a^{2w}(x) &= i\frac{w}{4}(a^w)^2 e^{i(2\beta^w-\beta^{2w})x}\varepsilon_0\int E_z^{2w*}(E_z^w)^2 d_{33}(x,z)dz \end{aligned} \tag{4}$$

Here $a^w$, $a^{2w}$, $\beta^w$, $\beta^{2w}$, $E_z^w$, and $E_z^{2w}$ are the amplitudes, transmission constants, and $z$-components of the electric field of the FW ($w$) and SH ($2w$) of the LRSPPs, respectively. $d_{33}$ is the nonlinear coefficient of $LiNbO_3$. We can see that the phase mismatching is different for the FW ( $\Delta\beta_1 = \beta^{2w} - \beta^{w*} - \beta^w = \beta^{2w} - 2real(\beta^w)$ ) and SH ( $\Delta\beta_2 = 2\beta^w - \beta^{2w}$ ). It is impossible to realize $\Delta\beta_1 = \Delta\beta_2 = 0$ at the same time. However, the reciprocal vector $G_m$ determined by the period $\Lambda$ of PPLN does not affect the absorption of LRSPPs, implying that $G_m$ can only match the real part of $\Delta\beta_{1,2}$ and leave the imaginary part unaffected. Therefore, we can realize QPM of the LRSPPs with

$$G_m = \frac{2\pi}{\Lambda} = real(\beta^{2w}) - 2real(\beta^w). \tag{5}$$

Under this QPM condition, the transmission properties of the FW and SH in the LRSPPs have been simulated with Eq. (4) before in our previous theoretical work [22].

## 3. Experiment

### 3.1 Preparation of sample

From the Sellmeier equation [23], we can see that the dispersion curve of $LiNbO_3$ is flatter in the near-infrared region. At these frequencies, it is easier for $TiO_2$ to match the $n_e$ of $LiNbO_3$ at the FW and SH simultaneously. In our experiment, we choose 1550 nm as the FW, thus, 775 nm is the SH. The ferroelectric domain period can be calculated from Eqs. (1)-(3) with different Au film thicknesses under the QPM condition. Table 1 summarizes the results.

Optics EXPRESS

**Table 1. PPLN period versus Au film thickness under the QPM condition.**

| Au film thickness (nm) | PPLN period (μm) | Au film thickness (nm) | PPLN period (μm) |
|---|---|---|---|
| 1 | 18.91 | 11 | 14.57 |
| 2 | 18.79 | 12 | 13.95 |
| 3 | 18.52 | 13 | 13.37 |
| 4 | 18.24 | 14 | 12.82 |
| 5 | 17.85 | 15 | 12.25 |
| 6 | 17.40 | 16 | 11.72 |
| 7 | 16.85 | 17 | 11.21 |
| 8 | 16.32 | 18 | 10.73 |
| 9 | 15.72 | 19 | 10.27 |
| 10 | 15.15 | 20 | 9.84 |

To determine the period of PPLN in experiment, two issues should be considered. Firstly, as predicted in [22], the thickness of the Au film is crucial. If the Au film is too thick, the absorption of the SH will be too large and the SH will be too weak to be detected. In contrast, if the Au film is too thin (e.g., 1 or 2 nm), it will be impossible to deposit a continuous film. Secondly, the fabrication accuracy of PPLN is important. The lithography machine we use in the fabrication of PPLN is SF-100 XTREME (Intelligent Micro Patterning, LLC). The pixel size with a 4 × objective lens is 1.32 μm. The period of the PPLN should be $2m \times 1.32$ μm ($m$ is an integer). Structural errors will always exist during the manufacture of the sample. To acquire QPM, we choose 13.2, 15.84, and 18.48 μm as the period of PPLN, and 9 and 13 nm as the thickness of the Au film.

Electric field poling is used to fabricate PPLN [24]. After depositing a Cr electrode with the designed periodical structures on the + c face of the congruent $LiNbO_3$ of about 50 μm in thickness, an electric field slightly larger than the coercive field is applied to the crystal to carry out the poling process. Because the $LiNbO_3$ crystal we used is very thin, the voltage we use to invert the ferroelectric domain is about 1100 V, and we can safely realize this domain inversion process at room temperature.

Grating coupling is a method to excite SPPs [21]. Here, we fabricate subwavelength gratings in the Au film to excite LRSPPs and guide the SH to the detector. We first fabricated gratings with depths of hundreds of nanometers in PPLN and then deposited 9 or 13-nm-thick Au film, completing the Au grating. In our experiment, the grating period for 1550 nm to excite SPPs is 1.08 μm with an angle of incidence of 45° (Grating A in Fig. 2(a)), and that for 775 nm to guide SPPs vertically to the detector is 354 nm (Grating B in Fig. 2(a)). The duty ratio of the grating is 1:1 and the size is 10 μm × 10 μm. The distance between Grating A and Grating B starts from 30 μm, increases by 10 μm, and ends at 120 μm. The grating was fabricated by focused ion beam etching (FIB).

After fabricating the gratings, an Au film and $TiO_2$ layer were deposited by magnetron sputtering. To obtain a very thin Au film, the depositing speed was set as low as possible, and the thickness of the Au film was measured by atomic force microscopy. By depositing $TiO_2$ with different speeds, the RI of the $TiO_2$ layer varies in a wide range. The RI of $TiO_2$ was measured by a spectrophotometer. When the RI differences both at 1550 and 775 nm between $TiO_2$ and the $n_e$ of $LiNbO_3$ are modulated to no more than 0.02, $TiO_2$ will be deposited on our sample. The thickness of the $TiO_2$ we obtained is about 2.3 μm.

### *3.2 QPM measurement*

Figure 2(a) illustrates the experimental setup to carry out the QPM measurement. Light with a wavelength of 1550 nm from a femtosecond laser coupled into a fiber with an 10 × objective lens is divided into two parts with a 1/99 coupler. The “1” part is connected to a power meter

Optics EXPRESS

as a reference beam, while the "99" part is coupled to Grating A to excite the LRSPPs via a fiber taper (the size of the tapered tip is about 2–3 μm), which is 45° to the normal of the sample. The SH signal is guided vertically to a beam splitter via grating B. One part of the beam is detected by a spectrometer, and the other part is collected by a microscope. Aperture C is used to block the light from the environment. In fact, this is a confocal micro-Raman spectrometer (CMRS), which is very sensitive to SH signals.

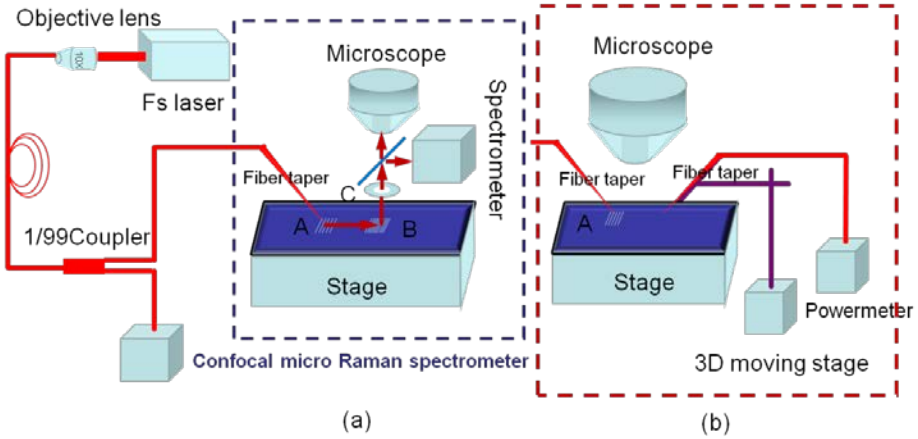


Fig. 2. Experimental setup to measure SH.(a) Confocal micro-Raman spectrometer. (b) Two-dimensional scanning system.

As mentioned above, we have fabricate samples with 6 configurations to testify the QPM SHG of LRSPPs. However, the SH signals of some samples are too weak to be well-recorded. Figure 3(a) presents the best results we obtained with these samples. The parameters of this sample are as follows: the period of the PPLN is 13.2 μm, the thickness of the Au film is 9 nm, the 1550-nm FW intensity transmitting through the fiber is 30 mW, the calculation time of the spectrometer is 1 s, and the RI differences between $TiO_2$ and the $n_e$ of $LiNbO_3$ are –0.02681 at 1550 nm and –0.00473 at 775 nm. We can see that the SH signal appears at a distance of 80 μm. The central wavelength is 776 nm, which is in accordance with the SH, and the full-width at half-maximum (FWHM) of this signal is 6.7 nm. As compared, the FWHM of FW is ~20nm.

There are parameter errors in the RI difference mentioned above in the fabrication process. Although QPM cannot be realized at 1550 nm, we can tune it to a wavelength that can satisfy the QPM condition. The wavelength of the FW changes, so the SH will also change and Grating B will not guide the SH vertically. Aperture C will block most of the SH signal, making the detected SH signal too faint. To overcome this drawback, we replace the CMRS in the frame of Fig. 2(a) with that of Fig. 2(b): another fiber taper scans pixel by pixel on the surface of the sample to collect the SH signal via a power meter. The step distance of the scanning is 3 μm. Figure 3(b) presents the scanning results. The wavelength of the FW is 1600 nm. Because the surface is far from the middle of the LRSPPs, the energy decays significantly, so the signal we collect at one pixel is very weak. From the left, the first spot, W, is the FW that decays very rapidly, and region X has no signal, which implies that the FW has been coupled to excite the LRSPPs. The second signal area, Y, agrees with where the strongest SH is detected by the CMRS (~80 μm). The third signal area, Z, is due to the QPM condition not being satisfied at 1600 nm. This configuration helps tune the wavelength to the QPM condition.

Optics EXPRESS

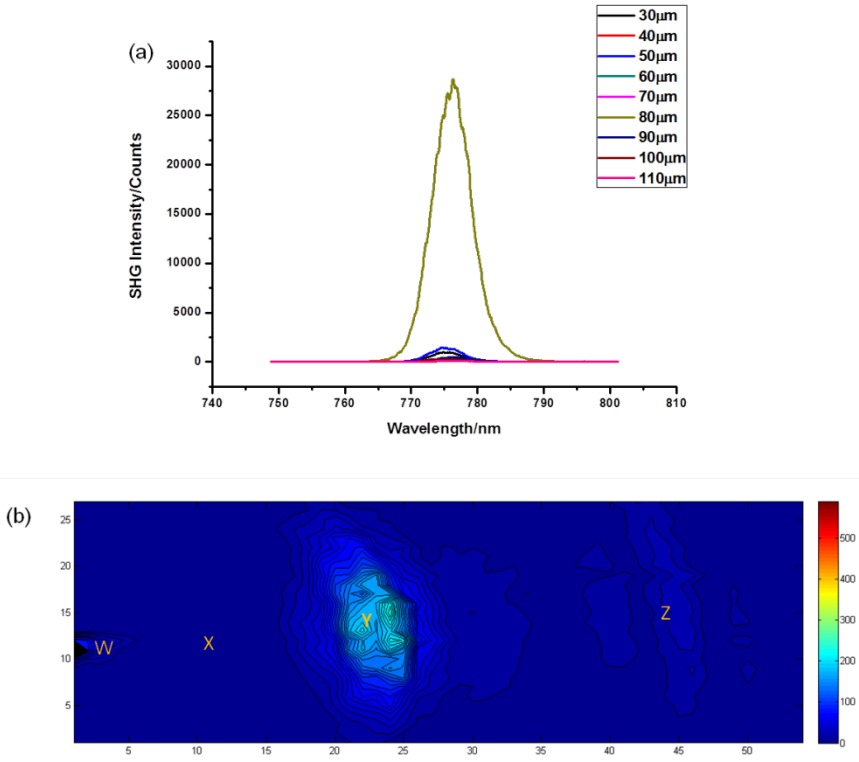


Fig. 3. (a) SH signal versus transmission distance, captured in Fig. 2(a). (b) Energy distribution on the surface of the sample collected by fiber taper scanning (Fig. 2(b)). The axis shows the step number. The coordinate is the step number of the moving taper, and the step distance of the scanning is 3 μm. The wavelength of the FW is 1600 nm.

In our experiment, we tuned the pump wavelength to acquire the highest SHG efficiency. Then we define the central wavelength as the QPM wavelength. As shown in Fig. 4(a), 1600 nm can be treated as the FW wavelength under QPM condition. The parameters of this sample are as follows: the period of the PPLN is 15.84 μm, the thickness of the Au film is 9 nm, the 1600-nm FW intensity transmitting through the fiber is 30 mW for Fig. 4(b), the calculation time of the spectrometer is 10 s, and the RI differences between $TiO_2$ and the $n_e$ of $LiNbO_3$ are –0.00223 at 1550 nm and 0.02108 at 775 nm. As predicted, the SH signal is lower than that captured with the CMRS in Fig. 2(a). To acquire the QPM condition, we tune the wavelength of the FW to 1600 nm. With the scanning system in Fig. 2(b), after finding the pixel with the largest signal, we keep the collecting fiber taper stable, change the light intensity coupled to the fiber with an attenuator, and read the numbers from the reference power meter and SH power meter. The SHG is quadratically nonlinear, so we fit the numbers with a quadratic equation. As mentioned above, the SH signal we collected at the surface of the sample with the scanning system is much smaller. There should be a basic FW intensity so the SH signal can reach the surface and be collected. Therefore, the equation should be $y = B_2(x + x_0)^2 + y_0$, where $x_0$ is the basic FW intensity and $y_0$ is a compensation term. Thus, we can fit it with the equation described in Table 2, which lists the fitting parameters, and the curve is shown in Fig. 4(c). As we can see, the statistically adjusted R-squared value is 0.99777, which is a very accurate result.

Optics EXPRESS

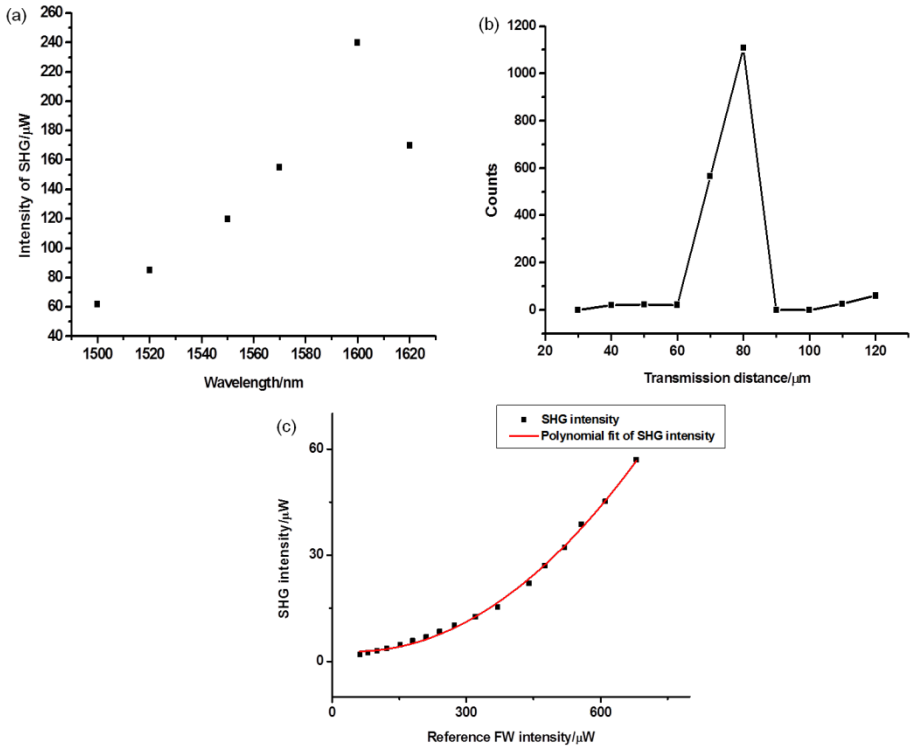


Fig. 4. QPM results. (a) The intensity of SH vs. the FW wavelength. (b) SH captured by the CMRS in Fig. 2(a). (c) SH collected by the scanning system in Fig. 2(b).

**Table 2. Parameters of the quadratic fitting of SH versus reference FW.**

Fitting equation: $y = B_0 + B_1 \bullet x + B_2 \bullet x^2$

| $B_0$ value | $B_0$ error | $B_1$ value | $B_1$ error | $B_2$ value | $B_2$ error | Statistically adjusted R-squared value |
|---|---|---|---|---|---|---|
| 3.1902 | 0.65229 | –0.01433 | 0.00451 | $1.37 \times 10^{-4}$ | $6.24 \times 10^{-6}$ | 0.99777 |

## 4. Discussion

### *4.1 Transmission distance and efficiency of the SHG of LRSPPs*

In a previous theoretical paper [22], the efficiency of the SHG of LRSPPs was reported to be very high, about 15.2%, and the intensity reached a maximum at about 500 μm. Compared with the results of slot waveguides in [16] and 2-D photonics crystal in [19], their mechanisms are different. Although LRSPP has higher loss, its sample structure is relatively simpler. In our experiment, with a 30-mW FW incidence, the largest SH signal, captured in Fig. 2(a), is at the maximum level the spectrometer could detect. Further, the maximum intensity of the SH appears at 80 μm, no more than 100 μm. We think there are several reasons for this phenomenon: (1) Only TM waves can excite LRSPPs. Although the light from the femtosecond laser is polarized, the polarization ratio is not very high, and the polarization of the FW coupled to the fiber taper is very sensitive and easy to change by the circumstance, so the TM part of the FW to excite the LRSPPs is smaller than that obtained via the power meter (30 mW). (2) The coupling efficiencies of the couple-in at Grating A and couple-out at Grating B greatly decrease the SH signal we detected with the spectrometer. (3) The RI of $TiO_2$ does not exactly match with the $n_e$ of $LiNbO_3$, which makes the mode of the

Optics EXPRESS

SPP not exactly symmetrical on both interfaces of the Au film, decreasing the transmission distance and intensity of the SH of the LRSPPs. We have simulated the SHG with RI mismatch, and found the maximum index mismatch for the FW and SH are ± 0.007 and ± 0.04, respectively, when LRSPPs can be supported. If the RI difference are 0.02 for both FW and SH, the mode profile for FW is not stable any more, while we still may obtain the frequency doubled LRSPPs. From our theoretical estimation, the peak efficiency comes out at a much shorter propagation length (~89.5 μm where the highest SH signal appears) and weaker SH intensity (20.3% of the largest SH intensity under RI match condition). (4) The permittivity of the bulk Au and Au film of about 10 nm in thickness is different. Because it is too thin, and many bubbles are present within it, the Au exhibits much more absorption. This shortens the transmission distance significantly and simultaneously decreases the SHG efficiency. (5) The SH from Grating B is a diverging beam. When it passes aperture C and travels a long distance to the detector, considerable energy is blocked. Thus, the results we obtained from the spectrometer does not represent exactly the intensity of the SH; the results are much smaller.

### *4.2 RI-matching layer: $TiO_2$*

The perfect RI material for LRSPPs in this study is $LiNbO_3$. Several methods have been reported to fabricate single-crystal $LiNbO_3$ film, such as crystal ion slicing [25,26] and magnetron sputtering [27]. The $LiNbO_3$ film made by crystal ion slicing is a single crystal, but until now, we have not been able to adhere it to a $LiNbO_3$ substrate with an Au film of about 10 nm in thickness without any glue or other material. In addition, the $LiNbO_3$ film made by sputtering is barely a single crystal. $TiO_2$ can be deposited easily and exhibits good adhesion with the $LiNbO_3$ substrate. Its RI can be modulated to the range of the $n_e$ of $LiNbO_3$ with different sputtering speeds. However, $TiO_2$ is hydrophilic [28], so steam will be absorbed by its surface and the RI will increase. When the RI changes significantly, LRSPPs cannot be excited, because the frequency is beyond the cut-off frequency of LRSPPs [21]. In our experiment, the LRSPPs can last for about two weeks. In this paper, we demonstrate the possibility of the QPM SHG of LRSPPs. A better RI-matching layer could improve this phenomenon greatly, both in the transmission distance and SHG efficiency.

### *4.3 Future research and applications*

This paper is a basic process in physics. Several photonic integrated devices can be realized with this phenomenon, such as waveguides and resonators. LRSPPs could also have applications in all-optical switching at telecommunication wavelengths [29]. The multi-wavelength nonlinear generation of LRSPPs can be realized by designing moderate ferroelectric domain structures [30]. With this, we can realize multi-color metasurface holography [31], which will greatly increase the efficiency. This process can enable attractive applications in nonlinear metamaterial [32] and quantum plasmonics [8]. For example, with the down-conversion nonlinear process, SPP entangled source may be provided [33, 34].

## 5. Conclusions

In this study, we experimentally demonstrate the QPM SHG of LRSPPs. The efficiency and transmission distance are much higher than those of LSPs. However, because the RI of $TiO_2$ is not exactly matched with $n_e$ of $LiNbO_3$, the transmission distance and the SHG efficiency are not as large as predicted with theory. With a better RI matching material, the transmission distance and the SHG efficiency can be improved greatly. This phenomenon may find promising applications in nonlinear metasurface holography and quantum plasmonics.

## Funding

National Science and Technology Major Project (2017YFA0303700) and National Natural Science Foundation of China (NSFC) (Nos. 61435008, 61490712 and 11604144).

Optics EXPRESS

## Acknowledgments

We thank microfabrication center, National Laboratory of Solid State Microstructures, Nanjing University for their technical support on the manufactory of PPLN. We also thank Qianjin Wang from nanofabrication characterization center, National Laboratory of Solid State Microstructures, Nanjing University for his support on FIB. Finally, we gracefully thank the support from Suzhou nanofabrication facility of SINANO, CAS, for the deposition, characterization of Au and $TiO_2$.